









High-order replica bands in monolayer FeSe/SrTiO₃ revealed by polarization-dependent photoemission spectroscopy

Chong Liu ^{1,2}, Ryan P. Day^{1,2}, Fengmiao Li ^{1,2}✉, Ryan L. Roemer ^{1,2}, Sergey Zhdanovich ^{1,2}, Sergey Gorovikov³, Tor M. Pedersen ³, Juan Jiang⁴, Sangjae Lee⁵, Michael Schneider ^{1,2}, Doug Wong^{1,2}, Pinder Dosanjh^{1,2}, Frederick J. Walker⁴, Charles H. Ahn^{4,5}, Giorgio Levy^{1,2}, Andrea Damascelli ^{1,2}, George A. Sawatzky^{1,2} & Ke Zou ^{1,2}✉

The mechanism of the enhanced superconductivity in monolayer FeSe/SrTiO₃ has been enthusiastically studied and debated over the past decade. One specific observation has been taken to be of central importance: the replica bands in the photoemission spectrum. Although suggestive of electron-phonon interaction in the material, the essence of these spectroscopic features remains highly controversial. In this work, we conduct angle-resolved photoemission spectroscopy measurements on monolayer FeSe/SrTiO₃ using linearly polarized photons. This configuration enables unambiguous characterization of the valence electronic structure with a suppression of the spectral background. We consistently observe high-order replica bands derived from various Fe 3*d* bands, similar to those observed on bare SrTiO₃. The intensity of the replica bands is unexpectedly high and different between *d*_{xy} and *d*_{yz} bands. Our results provide new insights on the electronic structure of this high-temperature superconductor and the physical origin of the photoemission replica bands.

¹Quantum Matter Institute, University of British Columbia, Vancouver, BC, Canada. ²Department of Physics and Astronomy, University of British Columbia, Vancouver, BC, Canada. ³Canadian Light Source, Saskatoon, SK, Canada. ⁴Department of Applied Physics and Center for Research on Interface Structures and Phenomena, Yale University, New Haven, CT, USA. ⁵Department of Physics, Yale University, New Haven, CT, USA. ✉email: fengmiao.li@qmi.ubc.ca; kzou@phas.ubc.ca

Since its discovery in 2012¹, monolayer (ML) FeSe grown on a SrTiO₃ (STO) substrate has drawn much attention. In addition to a superconducting transition temperature (T_c) over five times its bulk counterpart^{1,2}, FeSe/STO stands out amongst all iron-based superconductors, with both the largest superconducting energy gap of ~15–20 meV and the highest gap opening temperature of ~60–70 K^{2–4}. Previous angle-resolved photoemission spectroscopy (ARPES) work revealed that ML FeSe on STO is doped with ~0.12 electrons per Fe atom, transferred from the STO substrate^{3,4}. Although a similar electron doping drives an enhanced superconductivity also in many other FeSe-based systems^{5–7}, this mechanism alone was thought to be insufficient to explain the specifically large energy gap of FeSe/STO.

In pursuit of possible supplementary mechanisms by which the enhanced superconductivity in FeSe/STO is supported, interfacial electron-phonon coupling (EPC) has been of primary consideration^{8–10}. This is largely due to the observation of replica bands in the ARPES data. In addition to the primary photoelectron spectra, secondary intensity peaks which replicate the dispersion of the former can be identified at higher binding energies by a shift of ~90–100 meV^{8,11}. This is close to the energy of the STO's longitudinal optical phonon or Fuch–Kliwer (FK) phonon mode^{9,12}. Hence the replica bands were interpreted at first as the result of forward scattering of Fe 3*d* electrons by the STO phonons: a hallmark of strong EPC¹³. Recently the energy separation between the replica and principal peak was found to be slightly larger than the phonon energy, which was explained in the picture of EPC¹⁴. A connection was also drawn between the superconducting gap size and the replica peak amplitude, but this claim remains difficult to substantiate because of the complicated energy- and momentum-dependent photoelectron background signal.

Despite the attractive simplicity of the EPC argument, there are important concerns regarding the viability of this explanation for the replica features and their purported connection to high- T_c superconductivity¹⁵. One possible alternative considers extrinsic photoelectron energy loss processes¹⁶. In this scenario, the escaping photoelectrons interact with a time-dependent electric field from the STO substrate via a strongly coupled FK surface phonon at momentum $q = (0, 0)$. This interpretation has support from high-resolution electron energy loss spectroscopy (EELS) performed on STO^{12,17} at comparable incident energies and angles to those used in the ARPES measurements. This would imply that there is no direct connection between EPC and the replica bands, although EPC may still be relevant to the material's properties.

On the other hand, a bulk compound (TBA⁺)FeSe, where organic tetrabutyl ammonium molecules are intercalated in between FeSe layers, is reported to have a T_c of 43 K and a pseudogap up to 60 K¹⁸, comparable to FeSe/STO. The results have brought new debate on the role of the substrate in the superconductivity.

As FeSe/STO has demonstrated that interfacial engineering promises a viable route toward the enhancement of T_c in unconventional superconductors, an understanding of the physical mechanism involved is of central importance to the field. It is essential to ascertain whether the replica features observed in photoemission are indicative of EPC and its pivotal role in the physics of this material, or if this is merely an artefact of the experimental configuration detracting from the subject of interest.

To pursue this goal, further ARPES measurements are required. Challenges that have limited the progress come from not only the strict growth conditions that are necessary to ensure optimal superconductivity and clear replica bands^{19–21}, but also

the nature of the electronic states in FeSe/STO. On account of the strong correlations in this material²², the electron removal spectral function observed experimentally is broad, with extensive energy dependence, well beyond the sharp quasiparticle features familiar from bulk FeSe²³. This is further complicated by the presence of a substantial energy and momentum-dependent background. Near the chemical potential, where several bands of distinct orbital characters disperse through the same regions of energy and momentum, the usual inelastic background signal is supplanted by the tails of spectral features associated with different electron bands. Considering the objective of resolving individual replica bands and their relative intensities, this represents a formidable practical challenge to the unambiguous characterization of the ARPES spectra in FeSe/STO.

In this work, to address this challenge, we carry out synchrotron-based ARPES measurements with high energy and momentum resolution, using linearly polarized photons. As the familiar dipole selection rules impose strict constraints on the spatial symmetry of the electronic eigenstates observed via photoemission^{24,25}, the correct choice of polarization enables us to select specific bands of interest, suppressing contributions from nearby states entirely. Through application of this approach, we are able to observe replica bands at both the M and Γ points of the Brillouin zone (BZ), largely suppressing contributions from other nearby states. As the replica features are related to the excitation of a quantized bosonic mode, one should in principle observe higher-order replica features, with kinetic energies further reduced by multiples of the mode energy. Indeed, in addition to the first-order replica bands, we observe higher-order ones, and successfully extract the relative peak amplitudes. Without the complications of a pronounced background signal, we identify replica intensities in great excess of those reported previously, calling into questions about the physical origin of these features.

Results

ARPES on ML FeSe/STO with polarized photons. As illustrated in Fig. 1a, in the 2-Fe unit cell imposed by the glide-plane of the FeSe crystal, the Fermi surface of FeSe/STO is characterized by two crossed elliptic pockets centered at the M point²⁶. As the low-energy electronic structure is well represented by the bands near Γ and M, we focus our attention on the two cuts identified in Fig. 1a.

The ML FeSe films presented here are in the optimally doped and superconducting state (see “Methods” section, Supplementary Fig. 1, and ref. 20 for details of the sample growth). The doping level determined from the size of the electron pocket is ~0.11 electrons per Fe, while the superconducting gap is ~15.0 meV extracted from the energy distribution curve (EDC) at the Fermi momentum (Supplementary Fig. 2a), indicating high sample quality.

Our experimental geometry is sketched in Fig. 1b, where the emission plane coincides with the (110) mirror plane of FeSe lattice that is parallel to the nearest Fe–Fe direction, as confirmed by the low-energy electron diffraction (LEED) pattern (Supplementary Fig. 1c). The photoemission matrix element, dependent on the photon polarization and the initial and final electron wave functions, is important in determining the ARPES intensity²⁴: for p (s) geometry where the photon polarization vector is parallel (perpendicular) to the mirror plane, only even (odd) initial wave functions will be detected. This provides an experimental means by which closely spaced bands of particular orbital characters or parities can be addressed or suppressed selectively in the photoemission signal. The selection rules lead to a pronounced

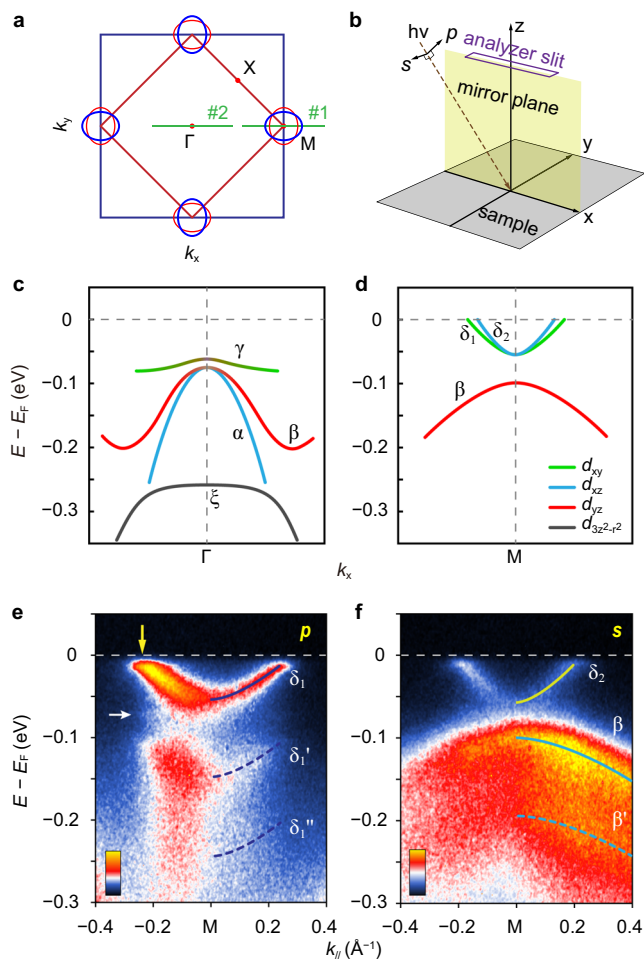


Fig. 1 ARPES characterization with polarized photons. **a** The 2-Fe (red square) and 1-Fe (blue square) Brillouin zones (BZs), and the sketch of Fermi surfaces (blue and red ellipses) of monolayer FeSe/STO²⁶. The green lines are the two cuts for the ARPES in Figs. 1–4. **b** Experimental geometry for linear polarization-dependent ARPES, where *p* (*s*) indicates the electric field of incident photon is parallel (perpendicular) to the emission plane defined by the analyzer slit. **c, d** Schematic diagram of band structure and orbital characters of monolayer FeSe/STO at Γ and M points, respectively, as determined by this ARPES study and in agreement with refs. 26,27. Here we use the same coordinate system as in **b** to define the *d* orbitals, i.e., *x* and *y* along the nearest Fe–Fe directions. Photoemission maps along cut #1, with 24 eV photons in *p* polarization (**e**) and *s* polarization (**f**). The solid and dashed curves indicate principal and replica bands with ~90 meV intervals, respectively. The white arrow indicates the other set of replica band at ~60 meV below the principal band. The yellow arrow indicates the Fermi momentum of the δ_1 band, where a superconducting gap is opened.

suppression of spectral background, enabling improved characterization of the replica bands.

From previous ARPES measurements^{26,27}, we expect four bands (α , β , γ and ξ) at Γ point (Fig. 1c) and three bands (δ_1 , δ_2 , and β) at M point (Fig. 1d) near Fermi level, consisting of different Fe 3*d* orbitals. In our *p*-polarized measurement, as shown in Fig. 1e, only one electron-type quasiparticle band δ_1 is visible at M point. Two replica bands, δ_1' and δ_1'' , show up on top of a clean background, with similar dispersion to the principal band (see Fig. 1e). Due to the gap opening at the Fermi level, the band shows apparent back-bending behavior, which is directly inherited in the replica band (Supplementary Fig. 2b). δ_1 , δ_1' , and δ_1'' are separated by an energy of ~94 meV, corresponding to one of the FK phonon modes of STO²⁸. A faint replica band is

captured at ~60 meV below the principal band (marked by the white arrow in Fig. 1e), corresponding to the other FK phonon of STO²⁸. δ_2 and β bands, on the other hand, are probed with the *s* polarization in Fig. 1f. By considering the experimental geometry, the selection rules and the symmetry analysis of the *d* orbital wave functions of two inequivalent Fe sites with the mirror plane running through Se sites²⁹, we identify the orbital characters to be d_{xy} for δ_1 , d_{xz} for δ_2 , and d_{yz} for β , as shown in Fig. 1d^{22,27}. The synchronous polarization dependence of principal bands and their replicas rules out the suspicion that the replica bands are the quasiparticle bands of other orbitals³⁰.

High-order replica bands and their intensities. There are mainly two proposed mechanisms for the replica bands, intrinsic EPC⁸ versus extrinsic energy loss of photoemitted electrons¹⁶. In both scenarios, multiple discrete replica bands are expected. The energy of the *n*th replica lies at $E_{qp} - n \times E_{\text{phonon}}$, where E_{qp} is the energy of quasiparticle band and E_{phonon} the phonon energy, resulting from electrons exciting *n* phonons each. The intensity of the *n*th replica band should follow the Poisson distribution with zero temperature approximation^{31–33}:

$$I_n/I_0 = \eta^n/n!, \tag{1}$$

where I_0 is the principal band intensity, I_n is the *n*th replica intensity, and $\eta = I_1/I_0$ characterizes the interaction strength. At the sample temperature of 9 K, $k_B T = 0.8$ meV is much smaller than the E_{phonon} , which validates the Poisson distribution. Multiple replica bands have been reported experimentally for the two-dimensional electron gas of the anatase TiO₂³⁴ and SrTiO₃^{32,35}, but have not been evidenced in FeSe/STO so far.

Figure 2 shows ARPES results for δ_1 , δ_2 and β bands at the M point and their replicas in a wider energy range. The δ_1 band dominates the spectra at the M point with *p*-polarized light. In the integrated EDC (Fig. 2b), there is a principal peak and a pronounced replica peak with ~94 meV offset. The hump observed approximately at -0.25 eV is the hallmark of the second replica of the principal peak. Below -0.3 eV is a dome-shaped background whose intensity is strongly dependent on the photon energy and unrelated to the principal peak, as will be discussed later on. The tails and inelastic background from other bands constitute the majority of the signal in this regime, which requires subtraction from the total signal in order to estimate the peak intensity.

We first follow the background method that was used in refs. 8,14 with a spline interpolation curve that running through several anchor points at the local minima of the data (green line in Fig. 2b). The intensity ratio between the first replica peak and the principal peak η is fit to be 0.40, almost twice the largest value measured with unpolarized photons in ref. 14. With such a large η in Eq. (1), the second-order replica intensity should be $I_2 \approx 0.08 I_0$, whereas the fitting result is $I_2 \approx 0.04 I_0$. This suggests that using a spline interpolation for the background, which has no physical basis, is likely to be unsuitable for these data. In fact, there is not an apparent explanation for such a high, dome-shaped background in the energy range above -0.3 eV in the *p* polarization measurement, where the spectral weight from the β band has already been suppressed.

In pursuit of a more suitable and physically motivated choice, we adopt a Tougaard-type background with multiple-peak fitting (see “Methods” for details), as shown in Fig. 2c. The Tougaard background considers the inelastic scattering of the electrons, and is widely used in photoemission spectroscopy^{36,37}. The spectral lineshape after background subtraction is nicely fit to a principal peak along with three replica peaks that follow the relation in Eq. (1) with $\eta = 0.70$. We cut off at the third replica band, as

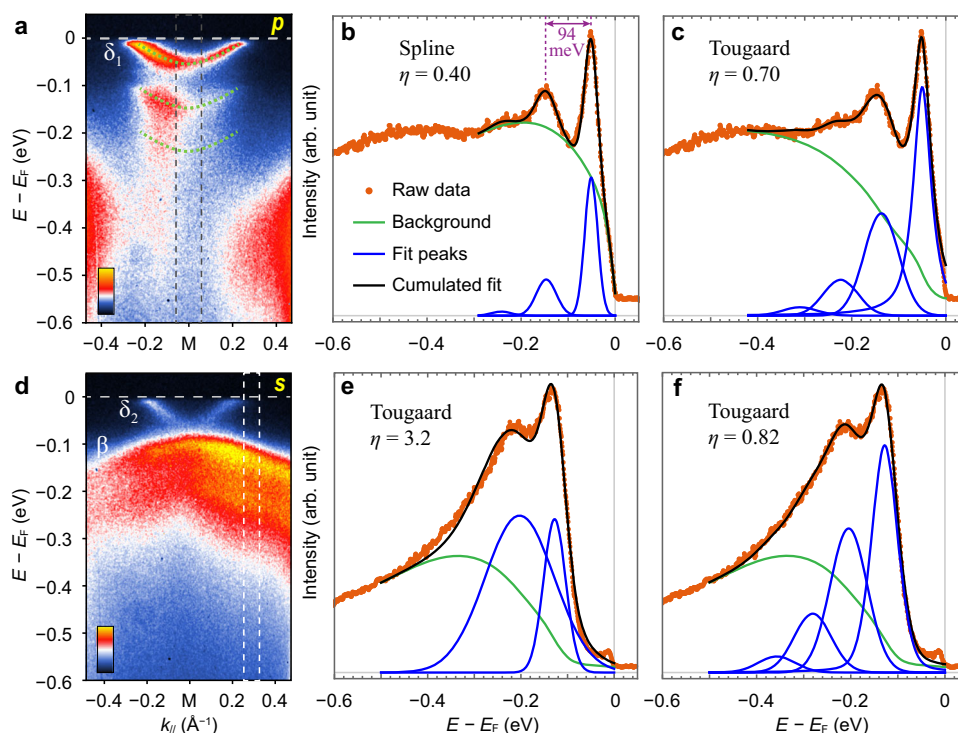


Fig. 2 Replica bands in monolayer FeSe/STO at the M point. **a** Photoemission intensity along cut #1 in Fig. 1a, measured with 24 eV photons in *p* polarization. **b** Energy distribution curve (EDC) at M, integrated over the momentum range indicated by the dashed rectangle in **a**. The background is modeled using a cubic spline interpolation and the data are fit to three Gaussian peaks; $\eta = I_n/I_0$ is the ratio of the areas of the first replica and the principal peak. **c** Same as **b**, but with the EDC fit with a Tougaard-type background and multiple peaks. The peak areas follow the Poisson distribution $I_n/I_0 = \eta^n/n!$ (see “Methods” section for details). **d** Same as **a** but for *s* polarization. **e** EDC integrated over the momentum range indicated by the white dashed rectangle in **d** so that the δ_2 band is excluded and only the β band contributes. The data are fit with a principal and a single replica peak which is unreasonably intense and broad. **f** Same as **e**, but with EDC now fit with a principal peak and three replica peaks, using the same method as in **c**.

additional replica peaks will carry <3% of I_0 . The same methodology has been applied to all other multiple-replica fittings in this work.

In the *s* polarization measurement, both δ_2 and β bands are manifested. Only the replicas of β band are visible while those of the δ_2 band, which are much weaker, overlap with the β band. We consider an integrated EDC acquired at a momentum beyond the extent of the δ_2 band to avoid its influence on the spectral fitting, as shown in Fig. 2d–f. The spectral shape is different from that of the δ_1 band in Fig. 2b, clear of the dome-shaped background from other bands. In this case the spline background that attaches to the data points is not feasible, and we return to using the Tougaard background for peak fitting. Although the second replica cannot be directly recognized in the EDC, a single replica peak fails to fit the data and exhibits an unreasonably high intensity with $\eta = 3.2$ and an extremely large linewidth (Fig. 2e), whereas the higher-order replicas must be involved when η is large according to Eq. (1). Ultimately, we successfully fit the data using a Tougaard background plus one principal peak along with three replica peaks with $\eta = 0.82$ (Fig. 2f). The η for the β band is higher than that of the δ_2 band, which holds true for different momentum windows being taken (Supplementary Fig. 3), implying a possible orbital dependence of the electron-phonon interactions.

Along cut #2 near the Γ point, several hole bands (α , β , and ξ) are observed (Fig. 3). In *p* polarization (Fig. 3a), the α band intensity is weaker and the strong ξ band lies below it, heavily superimposed over the replicas of the α band. By contrast, the α and ξ bands are eliminated with *s* polarization, while the β band and its replicas become most pronounced (Fig. 3b). The β band at Γ point can be fit similarly to our procedure at the M point and η

is also 0.82 (Fig. 3c), adding confidence in this choice of fitting. Remarkably, the multiple replica features and the η value are similar to that observed on an annealed bare STO surface³², hinting at a common physical origin.

Fitting of polarization-mixed data. To further demonstrate the advantage of our polarization-dependent strategy, we contrast our fitting results against those derived from unpolarized data. To accommodate a direct comparison, we sum over the intensity maps from the *p* and *s* polarizations to mimic the data obtained with unpolarized light (Fig. 4a) and take the integrated EDC around the M point (Fig. 4b). The results become similar to those in ref. 14 obtained with unpolarized photons, indicating the role of the polarization-dependent background in the anomalously small values of η reported previously.

Due to the coexistence and overlapping of the δ and β bands in a narrow energy range, the peak features are obscured by the large total signal, ultimately resulting in an underestimation of the replica intensity η when the spline background is used for peak fitting. In line with ref. 14, the η extracted from polarization-mixed data is not larger than 0.2 (Fig. 4b), while η is ~ 0.4 and by a factor of two higher for the polarized data (Fig. 2b), both with spline background. On the other hand, although the Tougaard background plus two groups of peaks manage to fit the polarization-integrated data (Fig. 4c) with $\eta = 0.82$, which is similar to that in Fig. 2f, an undesirable increase in the number of parameters ensues due to the complicated spectral components. The contrast between Figs. 2 and 4 demonstrates the significance of photon-polarized ARPES for more reliable characterization on the replica bands of FeSe. We also note that the background

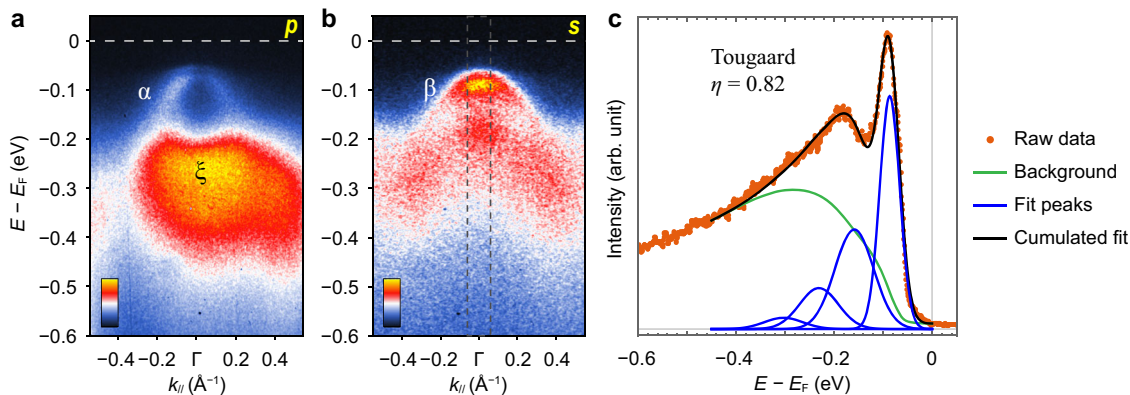


Fig. 3 Replica bands in monolayer FeSe/STO at the Γ point. **a** Photoemission intensity along cut #2 as indicated in Fig. 1a, measured with 24 eV photons in *p* polarization. **b** Photoemission intensity along cut #2 in Fig. 1a, measured with 50 eV photons in *s* polarization. **c** EDC at Γ , integrated over the momentum range indicated by the dashed rectangle in **b**. The data are fit with the same method as in Fig. 2f.

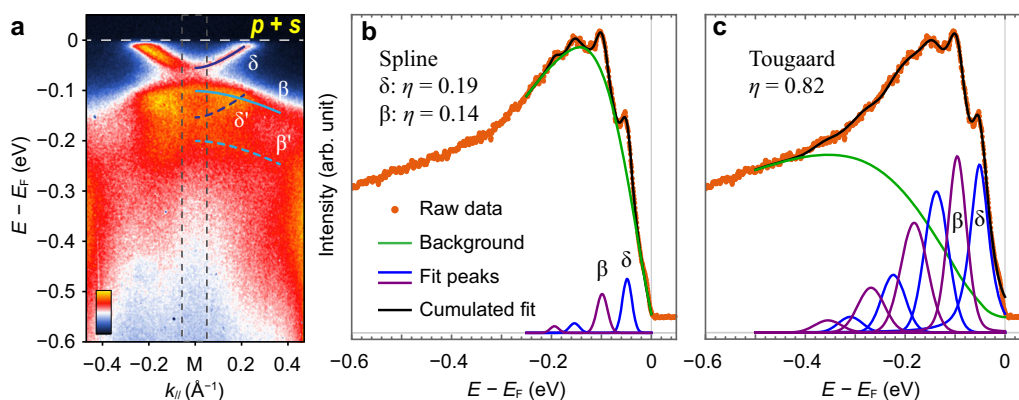


Fig. 4 Fitting ARPES results with mixed polarization. **a** Sum of the APRES maps around M point taken in *p* and *s* polarizations (Fig. 2a, d). **b** EDC integrated over the momentum range indicated by the dashed rectangle in **a**. The background is modeled using a cubic spline interpolation. The data are fit to four Gaussian peaks, corresponding to δ and β bands and their replicas. **c** Same data as **b**, but fit with a Tougaard background and two sets of multiple peaks for the δ and β bands, respectively.

method such as the spline that cannot yield consistent results between different measurements appears to be less suitable for quantitative and delicate analysis.

Photon energy/emission angle-dependent ARPES results. In the photoelectron energy loss process, the probability of generating an excitation is inversely proportional to the electron momentum perpendicular to the surface, *i.e.*, $\eta \propto 1/k_e \cos(\theta)$, where k_e and θ are the wave vector and escaping angle of the emitted electron relative to the surface normal, respectively. k_e is dependent on incident photon energy E_{photon} , and θ is dependent on both k_e and the measured in-plane momentum k_{\parallel} in the reciprocal space. For the 94 meV FK phonon, the derived η for various E_{photon} and high-symmetry points of BZ (Fig. 5a) are shown in Fig. 5b. The replica intensity increases with decreasing E_{photon} or increasing θ , which is distinguished from intrinsic EPC scenario where no variation of η is expected.

In reality, however, although photon polarization has suppressed a great portion of background observed in previous experiments, we found that a complicated E_{photon} -dependent (Fig. 5d) and θ -dependent (Fig. 5e–h) background persists, due to the neighboring *d* bands, the inelastic scattering of photoelectrons, or Debye–Waller effects on photoemission matrix elements³⁸. In addition, the photoemission intensity drops off extremely fast in the high BZs approaching grazing angles (Fig. 5f, h). The unpredictable evolution of the background with

measurement parameters makes it arduous to determine the intrinsic difference of replica band intensity for different E_{photon} or θ .

Discussion

We have shown that the measurement conditions have great impacts on the photoemission spectra, and certain parameters are preferable to obtain high signal-background ratio for replica bands, as summarized in Table 1. The background model, the peak lineshape, and the fitting parameters still undoubtedly influence the extracted replica amplitude η reported here. On the other hand, our methodology with carefully chosen photon energy and polarization provides higher data quality. The η values exceed those reported previously (0.05–0.22) by a significant margin¹⁴, regardless of the background models. The high η value together with the high-order peaks indicates that the interaction from which the replica bands are derived must be strong. Furthermore, the replica intensity appears to have orbital dependence for d_{yz} band (β) and d_{xy} band (δ_1). These findings require a reconsideration of the proposed interpretations of the replica bands and their relation to the enhanced superconductivity in FeSe/STO.

The high η value is unexpected from the existing EPC and photoelectron energy loss theories. For the interfacial EPC model, the replica band intensity η is approximately proportional to the dimensionless EPC constant λ for $\lambda < 1$ ^{39,40}.

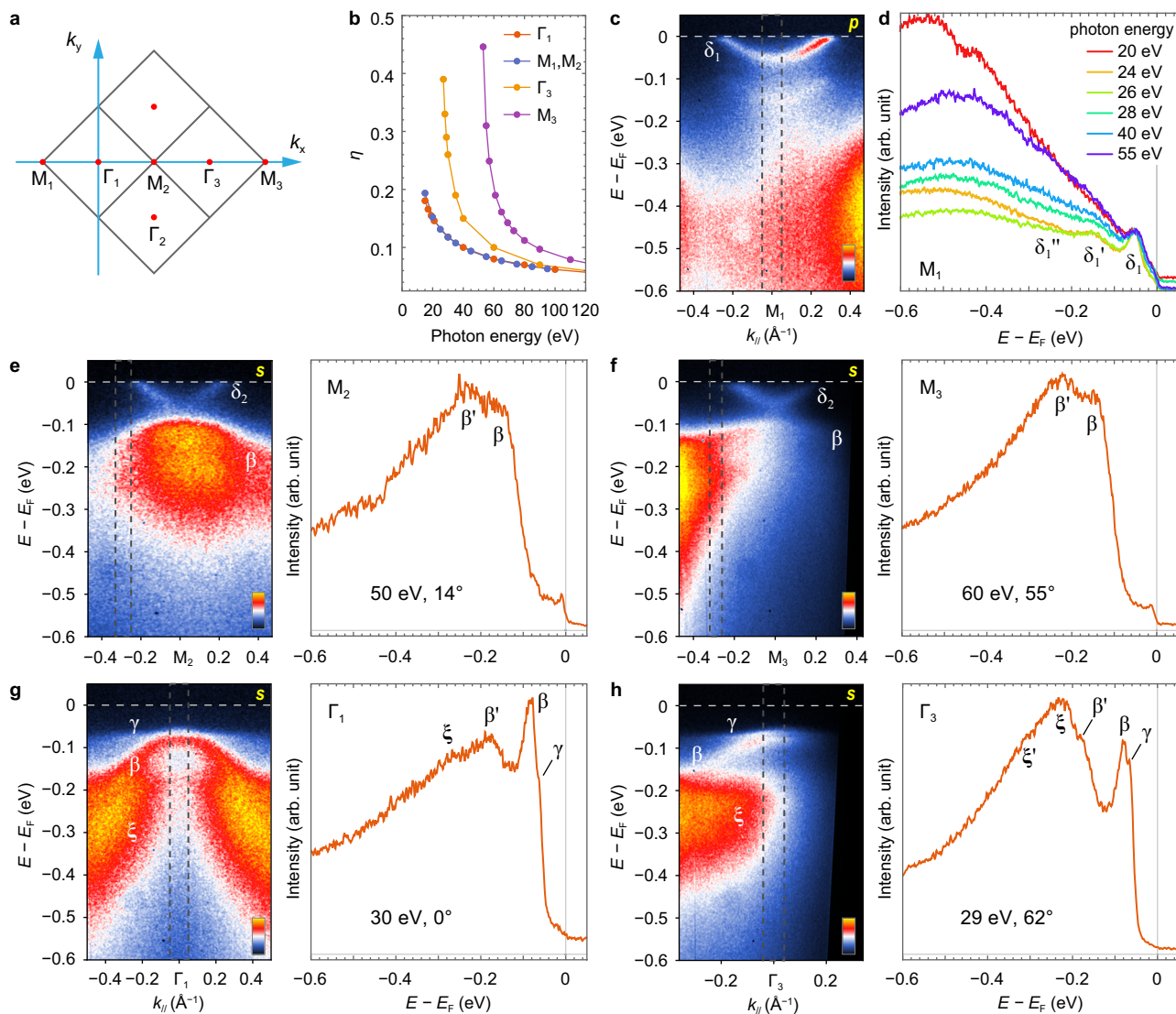


Fig. 5 Photon energy/emission angle-dependent ARPES results showing substantial variation of the background shape. **a** Extended reciprocal space and high-symmetry points of FeSe. The squares are BZ boundaries. **b** Calculated photon energy-dependent replica intensity at selected high-symmetry points, according to electron energy loss scenario. **c** ARPES map around M_1 point measured with p -polarized, 26-eV photons. **d** EDCs at M_1 taken with various photon energies, integrated over the momentum range indicated by the dashed rectangle in **c**. The curves are normalized by the principal peak maximum, and the background shows large variation with photon energy. **e–h** ARPES results at M_2 , M_3 , Γ_1 , and Γ_3 , respectively, measured with s -polarized photons. For each of **e–h**, the left panel is the intensity map, and the right is the integrated EDC, labeled with the photon energy and the emission angle of the electrons with respect to the sample normal. All measurements were taken with the analyzer slit along x direction.

Table 1 Parameters for high-visibility replica bands in the first BZ.

Band	Position in BZ	Polarization	Photon energy	η
d_{xy} (δ_1)	M point	p	24 eV	0.70
d_{yz} (β)	M point	s	24 eV	0.82
d_{yz} (β)	Γ point	s	50 eV	0.82

According to Migdal–Eliashberg theory⁴⁰, $\lambda = 0.2$ is enough to induce a T_c of 70 K, but the second-order replica bands should not be observable for λ below 0.3. For $\eta = \sim 0.7–0.8$, based on the quantum Monte Carlo simulation³⁹, λ would be $\sim 0.6–0.7$, much higher than expected from the T_c . In another theoretical study¹⁵, when Coulomb interaction amongst electrons in FeSe is taken into account, the phonon induced attractive potential is almost screened. This implies that the strong replica bands

cannot be solely attributed to EPC. In the photoelectron energy loss process, the escaping electron can interact with STO phonons over a longer distance¹⁶, so the ~ 0.5 -nm height of Fe atoms in ML FeSe relative to the STO surface^{41,42} is of little consequence here. This explains the comparable replica intensity measured from both ML FeSe/STO and bare STO. Nevertheless, the calculated η value for the measurements in the first Brillouin zoon is still smaller than 0.2 (Fig. 5b), distinct from our experimental results.

The different replica band intensity between d_{yz} and d_{xy} could be understood under EPC, when the electrons in the FeSe are coupled with the vertical dipole vibration of the oxygen atoms in STO⁹. On the other hand, photoelectrons undergo the energy loss process when traveling as plane waves in the vacuum subsequent to the electron removal event, so the orbital dependence is difficult to be settled in this framework. However, we cannot entirely exclude the possibility that the different η values between bands

result from the contamination of the spectra by adjacent bands or systematic error of background modeling or fitting. It is also possible that in reality, EPC and photoelectron energy loss both exist, leading to stronger replica bands than expected by either mechanism alone, and the contribution from EPC could carry some orbital dependence while the photoelectron energy loss remains independent.

After submission of this manuscript, we were aware of a relevant work⁴³ where replica bands of δ_1 are studied and the two major observations are (1) the replica band intensity has no dependence on the photon energy and (2) the energy separation between the first replica and the principal band (98 meV) is larger than the phonon energy obtained from EELS (94 meV). We note that the background used there is spline and the 2nd replica is not included in the fitting, different from this work. Besides, we do not observe a blue-shift of replica band on the same band in our data. In fact, the FK phonon energy itself depends on doping level and surface treatment of the STO¹² with a variation in the order of a few meVs. In EELS results, the replica peak energy of ML FeSe/STO is smaller than that of bare STO¹². Moving forward, further meticulously designed and extensive experiments and careful data analysis are required to provide solid evidence for the origin of replica bands and their relation with superconductivity in ML FeSe/STO. We recommend photon-polarized measurements as a necessary starting point for future studies.

Methods

Sample preparation. 0.05 wt% Nb:STO substrates (CrysTec GmbH) were etched in deionized water and 10% HCl, and annealed in O₂ at 1120 °C for 4 h in a tube furnace. ML FeSe films were grown in a Veeco GenXplor MBE system by codepositing Fe and Se on the substrates held at 420 °C²⁰. The flux ratio $\Phi_{\text{Fe}}:\Phi_{\text{Se}} \approx 1:5$. The base pressure of the chamber was $\sim 1 \times 10^{-10}$ Torr. Reflection high-energy electron diffraction was used to monitor the sample quality (Supplementary Fig. 1a, b). The samples were annealed at 480 °C for 3 h and then cooled down to room temperature and capped with 15-nm-thick Te and 5-nm-thick Se layers before being exposed to air. Before the ARPES measurements, in order to remove the capping layers and achieve the optimal superconducting state, the samples were gradually annealed to 450 °C and kept for ~ 5 h in the preparation chamber at pressure lower than 1×10^{-9} Torr. LEED patterns and X-ray photoelectron spectroscopy data were collected to verify the film quality.

ARPES. ARPES measurements were carried out on the Quantum Materials Spectroscopy Centre beamline at the Canadian Light Source, with vertically and horizontally polarized photons with energy ranging from 20 to 60 eV (see figure captions). Samples were measured at pressure lower than 5×10^{-11} Torr and a temperature of 9 K. The combined beamline-analyzer (Scienta R4000) resolutions in angle and energy are better than 0.1° and 9 meV, respectively.

EDC fitting. The superconducting gap is determined by fitting the symmetrized EDC to a spectral function with the simplified BCS self-energy⁴⁴ $\Sigma(\mathbf{k}, \omega) = -i\Gamma_1 + \Delta^2 / [\omega + \varepsilon(\mathbf{k}) + i\Gamma_0]$, where ω is the energy relative to Fermi energy, Δ is the gap size, Γ_0 is the inverse pair lifetime, Γ_1 represents the single-particle scattering rate, and $\varepsilon(\mathbf{k})$ is band dispersion [$\varepsilon(\mathbf{k}_F) = 0$]. For each of Figs. 2c, e, f, 3c, and 4c, the Tougaard-type background $T(E)$ is computed by the convolution of the EDC data $S(E')$ and a Gaussian energy loss cross-section function: $T(E) = A \int_E^\infty \exp\left[-\frac{(E-E')^2}{2\sigma^2}\right] S(E') dE'$, where A is the normalization factor and σ is the parameter that determines the shape of the curve. The data are fit to multiple peaks whose areas are constrained to follow the Poisson distribution $I_n/I_0 = \eta^n/n!$, where I_0 is the area of the principal peak and I_n is the area of the n th replica. The peak positions are constrained as $E_n = E_0 - n \cdot \Delta E$. The principal peak is fit with a Gaussian-Lorentz summed function. The replica peaks are fit with Gaussian functions. The full width at half maximum is constrained to be the same for the replica peaks of each band. The standard error of the estimate for η is smaller than 0.02 in all fittings.

Data availability

All data supporting the key findings of this study are available within the article and its Supplementary Information. All raw data generated during the current study are available from the corresponding authors on reasonable request.

Received: 29 December 2020; Accepted: 9 July 2021;

Published online: 28 July 2021

References

- Wang, Q.-Y. et al. Interface-induced high-temperature superconductivity in single unit-cell FeSe films on SrTiO₃. *Chin. Phys. Lett.* **29**, 037402 (2012).
- Zhang, W.-H. et al. Direct observation of high-temperature superconductivity in one-unit-cell FeSe films. *Chin. Phys. Lett.* **31**, 017401 (2014).
- He, S. et al. Phase diagram and electronic indication of high-temperature superconductivity at 65 K in single-layer FeSe films. *Nat. Mater.* **12**, 605–610 (2013).
- Tan, S. et al. Interface-induced superconductivity and strain-dependent spin density waves in FeSe/SrTiO₃ thin films. *Nat. Mater.* **12**, 634–640 (2013).
- Nekrasov, I. A., Pavlov, N. S., Sadovskii, M. V. & Slobodchikov, A. A. Electronic structure of FeSe monolayer superconductors. *Low. Temp. Phys.* **42**, 891–899 (2016).
- Wen, C. H. et al. Anomalous correlation effects and unique phase diagram of electron-doped FeSe revealed by photoemission spectroscopy. *Nat. Commun.* **7**, 10840 (2016).
- Niu, X. H. et al. Surface electronic structure and isotropic superconducting gap in (Li_{0.8}Fe_{0.2})OHFeSe. *Phys. Rev. B* **92**, 060504(R) (2015).
- Lee, J. J. et al. Interfacial mode coupling as the origin of the enhancement of T_c in FeSe films on SrTiO₃. *Nature* **515**, 245–248 (2014).
- Lee, D.-H. What makes the T_c of FeSe/SrTiO₃ so high? *Chin. Phys. B* **24**, 117405 (2015).
- Tang, C. et al. Interface-enhanced electron-phonon coupling and high-temperature superconductivity in potassium-coated ultrathin FeSe films on SrTiO₃. *Phys. Rev. B* **93**, 020507(R) (2016).
- Rebec, S. N. et al. Coexistence of replica bands and superconductivity in FeSe monolayer films. *Phys. Rev. Lett.* **118**, 067002 (2017).
- Zhang, S. et al. Lattice dynamics of ultrathin FeSe films on SrTiO₃. *Phys. Rev. B* **97**, 035408 (2018).
- Lee, D.-H. Routes to high-temperature superconductivity: a lesson from FeSe/SrTiO₃. *Annu. Rev. Condens. Matter Phys.* **9**, 261–282 (2018).
- Song, Q. et al. Evidence of cooperative effect on the enhanced superconducting transition temperature at the FeSe/SrTiO₃ interface. *Nat. Commun.* **10**, 758 (2019).
- Zhou, Y. & Millis, A. J. Dipolar phonons and electronic screening in monolayer FeSe on SrTiO₃. *Phys. Rev. B* **96**, 054516 (2017).
- Li, F. & Sawatzky, G. A. Electron phonon coupling versus photoelectron energy loss at the origin of replica bands in photoemission of FeSe on SrTiO₃. *Phys. Rev. Lett.* **120**, 237001 (2018).
- Conard, T., Philippe, L., Thiry, P. A., Lambin, P. & Caudano, R. Electron energy-loss spectroscopy and dynamics of SrTiO₃(100). *Surf. Sci.* **287–288**, 382–385 (1993).
- Kang, B. L. et al. Preformed Cooper pairs in layered FeSe-based superconductors. *Phys. Rev. Lett.* **125**, 097003 (2020).
- Li, Z. et al. Molecular beam epitaxy growth and post-growth annealing of FeSe films on SrTiO₃: a scanning tunneling microscopy study. *J. Phys. Condens. Matter* **26**, 265002 (2014).
- Liu, C. & Zou, K. Tuning stoichiometry and its impact on superconductivity of monolayer and multilayer FeSe on SrTiO₃. *Phys. Rev. B* **101**, 140502(R) (2020).
- Zou, K. et al. Role of double TiO₂ layers at the interface of FeSe/SrTiO₃ superconductors. *Phys. Rev. B* **93**, 180506(R) (2016).
- Mandal, S., Zhang, P., Ismail-Beigi, S. & Haule, K. How correlated is the FeSe/SrTiO₃ system? *Phys. Rev. Lett.* **119**, 067004 (2017).
- Rhodes, L. C. et al. Scaling of the superconducting gap with orbital character in FeSe. *Phys. Rev. B* **98**, 180503 (2018).
- Damascelli, A. Probing the electronic structure of complex systems by ARPES. *Phys. Scr.* **2004**, 61 (2004).
- Day, R. P., Zwartsenberg, B., Elfimov, I. S. & Damascelli, A. Computational framework chinook for angle-resolved photoemission spectroscopy. *npj Quantum Mater.* **4**, 54 (2019).
- Zhang, Y. et al. Superconducting gap anisotropy in monolayer FeSe thin film. *Phys. Rev. Lett.* **117**, 117001 (2016).
- Yi, M. et al. Observation of universal strong orbital-dependent correlation effects in iron chalcogenides. *Nat. Commun.* **6**, 7777 (2015).
- Zhang, S. et al. Role of SrTiO₃ phonon penetrating into thin FeSe films in the enhancement of superconductivity. *Phys. Rev. B* **94**, 081116(R) (2016).
- Brouet, V. et al. Impact of the two Fe unit cell on the electronic structure measured by ARPES in iron pnictides. *Phys. Rev. B* **86**, 075123 (2012).

30. Nekrasov, I. A., Pavlov, N. S. & Sadovskii, M. V. On the origin of the shallow and “replica” bands in FeSe monolayer superconductors. *JETP Lett.* **105**, 370–374 (2017).
31. Lambin, P., Vigneron, J. P. & Lucas, A. A. Computation of the surface electron-energy-loss spectrum in specular geometry for an arbitrary plane-stratified medium. *Comput. Phys. Commun.* **60**, 351–364 (1990).
32. Chen, C., Avila, J., Frantzeskakis, E., Levy, A. & Asensio, M. C. Observation of a two-dimensional liquid of Fröhlich polarons at the bare SrTiO₃ surface. *Nat. Commun.* **6**, 8585 (2015).
33. Ibach, H. Optical surface phonons in zinc oxide detected by slow-electron spectroscopy. *Phys. Rev. Lett.* **24**, 1416–1418 (1970).
34. Moser, S. et al. Tunable polaronic conduction in anatase TiO₂. *Phys. Rev. Lett.* **110**, 196403 (2013).
35. Wang, Z. et al. Tailoring the nature and strength of electron-phonon interactions in the SrTiO₃(001) 2D electron liquid. *Nat. Mater.* **15**, 835–839 (2016).
36. Tougaard, S. Quantitative analysis of the inelastic background in surface electron spectroscopy. *Surf. Interface Anal.* **11**, 453–472 (1988).
37. Tougaard, S. Practical guide to the use of backgrounds in quantitative XPS. *J. Vac. Sci. Technol. A* **39**, 011201 (2021).
38. Zhou, J. S. et al. Unraveling intrinsic correlation effects with angle-resolved photoemission spectroscopy. *Proc. Natl Acad. Sci. USA* **117**, 28596–28602 (2020).
39. Li, Z.-X., Devereaux, T. P. & Lee, D.-H. Electronic and phononic properties of a two-dimensional electron gas coupled to dipolar phonons via small-momentum-transfer scattering. *Phys. Rev. B* **100**, 241101(R) (2019).
40. Rademaker, L., Wang, Y., Berlijn, T. & Johnston, S. Enhanced superconductivity due to forward scattering in FeSe thin films on SrTiO₃ substrates. *N. J. Phys.* **18**, 022001 (2016).
41. Li, F. et al. Atomically resolved FeSe/SrTiO₃(001) interface structure by scanning transmission electron microscopy. *2D Mater.* **3**, 024002 (2016).
42. Peng, R. et al. Picoscale structural insight into superconductivity of monolayer FeSe/SrTiO₃. *Sci. Adv.* **6**, eaay4517 (2020).
43. Faeth, B. D. et al. Interfacial electron-phonon coupling constants extracted from intrinsic replica bands in monolayer FeSe/SrTiO₃. *Phys. Rev. Lett.* **127**, 016803 (2021).
44. Norman, M. R., Randeria, M., Ding, H. & Campuzano, J. C. Phenomenology of the low-energy spectral function in high-T_c superconductors. *Phys. Rev. B* **57**, R11093–R11096 (1998).

Acknowledgements

This research was undertaken thanks in part to funding from the Max Planck-UBC-UTokyo Centre for Quantum Materials and the Canada First Research Excellence Fund, Quantum Materials and Future Technologies Program. The work at the University of British Columbia was also supported by Natural Sciences and Engineering Research Council of Canada (NSERC), the Canada Foundation for Innovation (CFI), the British Columbia Knowledge Development Fund (BCKDF), and the Canada Research Chairs

Program (A.D.). The work at the Canadian Light Source was supported by CFI, NSERC, the National Research Council (NRC), the Canadian Institutes of Health Research (CIHR), the Government of Saskatchewan, and the University of Saskatchewan. The work at Yale University was supported by the U.S. Department of Energy (DOE), Offices of Science, Office of Basic Energy Sciences under Award No. DE-SC0019211.

Author contributions

F.L., G.A.S., and K.Z. proposed and designed this project. C.L. prepared the samples. C.L., R.P.D., F.L., R.L.R., J.J., and S.L. conducted the ARPES measurements. S.Z., S.G., T.M.P., M.S., D.W., P.D., G.L., and A.D. developed and maintained the QMSC beamline and ARPES system. C.L. and R.P.D. analyzed the data. C.L., F.L., F.J.W., C.H.A., A.D., G.A.S., and K.Z. discussed on the results. C.L., R.P.D., and K.Z. wrote the manuscript with comments from all authors.

Competing interests

The authors declare no competing interests.

Additional information

Supplementary information The online version contains supplementary material available at <https://doi.org/10.1038/s41467-021-24783-5>.

Correspondence and requests for materials should be addressed to F.L. or K.Z.

Peer review information *Nature Communications* thanks Yukiaki Ishida and the other, anonymous, reviewer(s) for their contribution to the peer review of this work.

Reprints and permission information is available at <http://www.nature.com/reprints>

Publisher's note Springer Nature remains neutral with regard to jurisdictional claims in published maps and institutional affiliations.



Open Access This article is licensed under a Creative Commons Attribution 4.0 International License, which permits use, sharing, adaptation, distribution and reproduction in any medium or format, as long as you give appropriate credit to the original author(s) and the source, provide a link to the Creative Commons license, and indicate if changes were made. The images or other third party material in this article are included in the article's Creative Commons license, unless indicated otherwise in a credit line to the material. If material is not included in the article's Creative Commons license and your intended use is not permitted by statutory regulation or exceeds the permitted use, you will need to obtain permission directly from the copyright holder. To view a copy of this license, visit <http://creativecommons.org/licenses/by/4.0/>.

© The Author(s) 2021